Finite Element Modeling and Experimental Characterization of Piezoceramic Frequency Steerable Acoustic Transducers

Finite Element Modeling and Experimental Characterization of Piezoceramic Frequency Steerable Acoustic Transducers

Masoud Mohammadgholiha[1*], Antonio Palermo[2], Nicola Testoni[3], Jochen Moll[4], and Luca De Marchi[1]

[1]Department of Electrical, Electronic, and Information Engineering, University of Bologna, Bologna, Italy

[2]Department of Civil, Chemical, Environmental, and Materials Engineering, University of Bologna, Bologna, Italy

[3]Advanced Research Center on Electronic Systems "Ercole De Castro" (ARCES), University of Bologna, Bologna, Italy

[4]Department of Physics, Terahertz/Photonics Group, Goethe University of Frankfurt am Main, Frankfurt, Germany

Abstract:

This paper presents a novel implementation of Frequency Steerable Acoustic Transducers (FSATs) for guided waves (GWs) inspections. Unlike the conventional phased array systems, which demand a large number of transducers and complex wiring, FSATs benefit from inherent directional properties for generation and sensing ultrasonic guided waves, resulting in significant hardware simplification and cost reductions for GWs-based systems. The FSATs exploit the frequency-dependent spatial filtering effect, leading to a direct relationship between the direction of propagation and the frequency content of the transmitted signal. The proposed Piezoceramic FSAT is fabricated through patterning the spiral electrodes on a Piezoelectric (PZT) plate bonded on a supporting aluminum plate. In light of the need to investigate the influence of the generated stiffness caused by the PZT plate on the coupling behavior between the FSAT and the aluminum plate, Finite Element (FE) simulations were carried out. Furthermore, experimental validations were conducted using a Scanning Laser Doppler Vibrometer (SLDV) to highlight the directional capabilities of such devices. The results show that the generation of directional GWs in a host structure is substantially improved thanks to the high actuation strength of Piezoceramic materials employed in the proposed transducer.

Keywords: Frequency Steerable Acoustic Transducers (FSATs), Guided Waves (GWs), PZT, Structural Health Monitoring (SHM), Transducer simulation.

1. INTRODUCTION

In recent years, Structural Health Monitoring (SHM) has gained momentum in civil, mechanical, and aerospace structures. As a key component of damage prognosis systems, SHM evaluates the health status of a structure and provides information about possible damages [1]. Among SHM techniques, ultrasonic Guided Waves (GWs) inspection has become a prominent and extensively-used option employed by numerous SHM systems [2], [3]. In the case of a plate-like structure, GW, and in particular Lamb waves, can propagate long distances along the plate and transmit information, which can be identified using a receiver mounted at a remote location on the structure [4]-[6]. The generation and sensing of GW can be implemented through piezoelectric transducers (PZT) to evaluate the existence of damage [7]-[9]. Numerous studies have been conducted on the use of PZT transducers in GW-based SHM and damage detection [10]-[15].

The incorporation of transducers with adjustable directional properties facilitates GW-based SHM techniques, allowing for surface scanning to locate possible damages. A well-established method for achieving this goal is beam steering by phased arrays [16], which is widely used in ultrasonic imaging and non-destructive evaluation (NDE) applications [17], [18]. However, GW testing through phased arrays requires a large number of PZT transducers, which is costly and complex [19], [20]. In order to overcome such drawbacks, alternative techniques featuring transducers with inherent beam steering capabilities started gaining interest [21]-[28]. Among others, recent studies demonstrated the ability to use frequency to control beam steering by designing Frequency Steerable Acoustic Transducers (FSATs) [29], [30].

The FSATs exploit the spatial filtering effect to generate/receive waves corresponding to the frequency of excitation/incoming wave. As a result, a unique relationship can be established between the direction of propagation and the frequency content of the transmitted/received signals [30]. An example of FSAT is the spiral-shaped transducer originally introduced in [31] and later fabricated on a PVDF substrate to experimentally investigate the directional GWs generation on a supporting aluminum plate [32]. However, the FSAT showed a limited directional performance due to the low actuation strength of PVDF, especially at high frequencies [33]. Hence, there is a need for improving the FSAT directional capabilities using a suitable material.

Piezoelectric ceramics (Piezoceramics) are an attractive alternative to PVDF and are widely used in GW sensing and actuation [34], [35]. The piezoelectric coupling coefficients of Piezoceramics are considerably higher than those of PVDF, ensuring the generation of higher stresses/strains when subjected to the same electrical field as PVDF [36]. Hence, Piezoceramics offers superior actuation strength for wave generation purposes [37]. Similarly, the voltage response of Piezoceramic sensors is much greater than that of PVDF under the same load condition [38], nearly 60 times higher, as reported in [39]. With this in mind, Piezoceramics are expected to outperform PVDF in terms of GW sensing and actuation, motivating a new research direction which focuses on the Piezoceramic-based FSATs.

This paper demonstrates the numerical implementation and experimental validation of a novel FSAT which is made of piezoceramic materials that enables beam steering with substantially higher accuracy than the previous PVDF examples. To achieve such performance improvements, considerations of the transducer thickness and the material properties in the FSAT design phase are of great importance. As discussed, the high piezoelectric constants of Piezoceramics provide a considerable actuation authority to the proposed FSAT. In addition, the elastic modulus and the thickness of the proposed Piezoceramic FSAT are greater than those of PVDF examples, increasing the transducer stiffness. Consequently, the higher stiffness leads to an increase in

rigidity in specific areas, i.e., the transducer domain. Such an effect leads to a completely different coupling behavior between the FSAT and the host structure, which is not taken into consideration in the original FSAT design concept [40]. On the other hand, a purely experimental approach in developing the new FSAT with such characteristics is time-consuming and expensive. An alternative approach adopted to address such concerns is the combination of experiments and a robust Finite Element (FE) simulation tool, which pave the way to achieve the desired performance [41].

This work is organized as follows: the FSAT principles of operations are reviewed in Section 2 along with a numerical analysis to show the influence of the transducer thickness. Section 3 describes the finite element simulation of FSATs using two different approaches. The fabrication process of FSATs as well as the experimental results are reported in section 4, followed by the conclusion in section 5.

2. SPIRAL FREQUENCY STEERABLE ACOUSTIC TRANSDUCERS FOR GUIDED WAVE ACTUATION

This section aims to first describe briefly the governing equations established for guided waves propagation through arbitrary shape transducers. The actuation capabilities of spiral FSATs are then illustrated through the definition of the frequency-based beam steering concept, which is used for the subsequent description of the transducer geometry. Finally, the influence of the transducer thickness and the material properties on the directivity pattern are investigated.

Following the theory presented in [42], the response given by an arbitrary piezoelectric patch Ω_p placed on an elastic medium at a certain point Q with position vector $\boldsymbol{r} = r\boldsymbol{u}$ (shown in Fig. 1), can be expressed as:

$$z(\boldsymbol{r}, \omega) = g_0(\omega) G(\boldsymbol{r}, \boldsymbol{x}, \omega) D(\omega, \theta) \tag{1}$$

where $z(\boldsymbol{r}, \omega)$ is the entire response at frequency ω, $g_0(\omega)$ defines the amplitude of the harmonic signal $g(t) = g_0(\omega) e^{-j\omega t}$ generated by the point sources considered inside the piezopatch, $G(\boldsymbol{r}, \boldsymbol{x}, \omega)$ is an appropriate Green's function representing the response to a unit point source, and $D(\omega, \theta)$ indicates the directivity function defined for the direction of transmission wave at angel θ. It should be noted that each infinitesimal actuation element $d\Omega$ is considered as a point source with the ability to generate a harmonic signal, which can be used to obtain the entire piezo-patch response through superposition principle. [42].

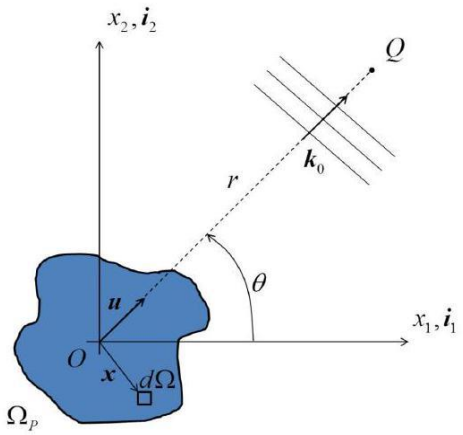

Figure 1: Plate with arbitrarily shaped piezoelectric actuator Ω_P bonded on the top surface [42]

The directivity function used in (1) can be computed as:

$$D(\omega,\theta)=\int_{\Omega_P} f(\boldsymbol{x})e^{-j\boldsymbol{k_0}(\omega)\cdot\boldsymbol{x}}d\Omega \tag{2}$$

in which, $f(\boldsymbol{x})$ indicates the load distribution function, i.e., the transducer shape and polarization, and $k_0(\omega)$ is the dispersion relation of the considered medium, which shows the frequency dependency of the directivity function. By utilizing the limited support of $f(\boldsymbol{x})$, (2) can be rewritten as:

$$D(\omega,\theta)=\int_{-\infty}^{+\infty} f(\boldsymbol{x})e^{-j\boldsymbol{k_0}(\omega)\cdot\boldsymbol{x}}d\Omega \tag{3}$$

which is identified as the spatial Fourier Transform (FT) of the function $f(\boldsymbol{x})$, enabling the calculation of the directivity patterns corresponding to different transducer shapes by estimating the FT pairs. To put it another way, considering D and f as an FT pair, it is beneficial to design the desired directivity function in D and then use the FT to generate the piezotransducer geometry which benefits such directional behavior [43]-[45]. To incorporate the described discussion into the FSAT design idea, the frequency-based beam steering concept is provided in the following.

The elasto-dynamic equations of motion governing guided wave propagation within a plate-like structure described before can be represented by a generic form as follows [40]:

$$P[z(x,\omega)]=f(x,\omega) \tag{4}$$

in which, z defines the plate displacement field response to a harmonic load distribution $f(x,\omega)$ at frequency ω. P denotes a differential operator defining the considered medium. Two in-plain coordinates defining the position vector $x=[x_1,x_2]$ are assumed to describe the considered location on the plate.

A 2-D Fourier transform (FT) can be used to solve (4), transforming it into the following algebraic form:

$$\hat{z}(k,\omega)=\hat{P}^{-1}(k,\omega)\hat{f}(k,\omega) \tag{5}$$

where $\hat{P}$ stands for the Fourier transform from space to wavenumber $k=[k_1,k_2]$ domain. As described in [40], the displacement amplitude can be maximized in certain directions by correctly adjusting the load distribution and excitation frequency. The load distribution $\hat{f}(k,\omega)$, which is defined by the spatial distribution of the applied load $f(x,\omega)$, is obviously maximum when:

$$\hat{P}(k,\omega)=0 \tag{6}$$

which corresponds to the dispersion relation of the considered medium. Thus, the maximum displacement output can be achieved when the load distribution intersects the medium's dispersion relation at wavenumber k^*, whose direction indicates the direction of waves generated in the plate. Therefore, in the actuation mode of FSAT performance, frequency-based beam steering is achieved by designing the transducer load distribution $\hat{f}(k,\omega)$ in such way that the direction of the generated waves can be controlled by varying the excitation frequency [40].

3. TRANSDUCER GEOMETRY DEFINITION

As discussed, the FSAT design concept is based on the frequency-dependent directivity idea, which proposes that the transducer load distribution can be properly specified in the wavenumber domain to derive

the corresponding geometry for the device using an inverse Fourier transform [40]. The shape-related spiral directivity function depicted in Fig. 2a, illustrates a continuous directivity distribution with respect to the frequency of radiation:

$$D[k_0(\omega),\theta] = -j\frac{a}{N}\sum_{n=1}^{N}\left[\frac{J_1(a|k_0-k_n|)}{a|k_0-k_n|)} - \frac{J_1(a|k_0+k_n|)}{a|k_0+k_n|)}\right] \tag{7}$$

where a indicates the patch radius in the spatial domain, $J_1(x)$ is the first order Bessel function, and k_n defines the wave vector associated with the angle θ_n, at which the $n-th$ maximum of the spiral transducer placed in the wavenumber domain (blue circles in Fig. 2a).

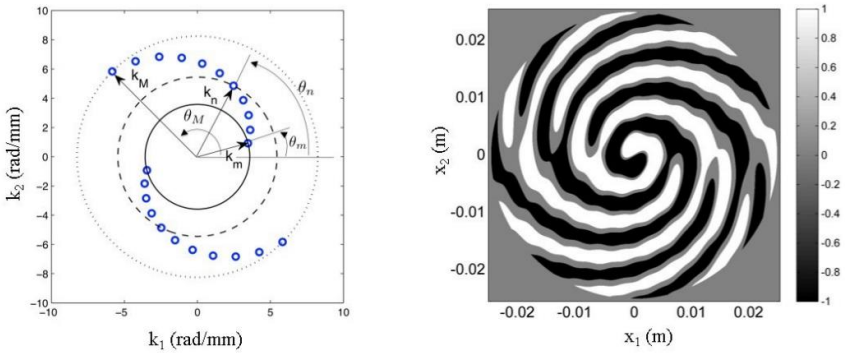

Figure 2: a) Spiral directivity in the wavenumber domain b) pattern of the designed electrodes [40]

Following the method described in [40], in order to obtain a frequency-directivity over the angular range $[\theta_m, \theta_M] \subseteq [0°, 180°]$, the FSAT should be designed in such a way that the maxima of the associated out-of-plane load distribution $\hat{f}(k,w)$ are placed into a spiral configuration in the wavenumber range $[k_m, k_M]$:

$$k_n = \left[k_m + (k_M - k_m)\frac{\theta_n - \theta_m}{\theta_M - \theta_m}\right](\cos\ \theta_n i_1 + \sin\ \theta_n i_2) \tag{8}$$

As illustrated in Fig. 2a, the wavenumber-spiral shape enables iso-frequency circles indicating dispersion relations for isotropic media to cross a single directivity maximum for a certain wave vector, thereby representing a single direction of sensing/transmission [46]. As it can be seen, the load distribution (blue circles) spans an area between θ_m to θ_M with three iso-frequency circles, whose radius indicates a specific wavenumber value. Therefore, increasing wavenumbers, and consequently frequencies, leads to radiation at increasing angles θ_n. It should be noted that the spiral configuration is determined by choosing a sequence of angular values θ_n in a way that discrete amplitude peaks are spaced by constant arclengths throughout the spiral [40]. The transducer geometry can then be obtained through a FT of the directivity function, as depicted in Fig. 2b.

4. INFLUENCE OF TRANSDUCER THICKNESS

The FSAT design procedure [40] described above is based on the analytical solution to predict the directivity pattern. As mentioned before, the dispersion curve of the propagation medium plays a significant role in the directivity computation. Indeed, since the direction of the generated waves is controlled by the excitation

frequency, the corresponding wavenumber obtained from the dispersion curve indicates the waves direction, as shown in Fig. 3. Therefore, a small change in the dispersion curve would result in significant differences in the wavenumber-frequency relationship.

The original analytical model used for directivity prediction [40] is not capable of taking the PZT thickness into consideration. In fact, the FSAT is considered as a zero-thickness transducer coupled with a host structure with a specific dispersion relation. However, findings of the present study reveal the significant contribution of the PZT thickness (hence PZT stiffness) on the FSAT directional performance. In order to account for the PZT thickness in the analytical model, a dispersion modification procedure was carried out through a Finite Element (FE) simulation. As described in [47], the infinite plate can be constrained to a unit cell representing the infinite-plate waveguide. In this regard, a three-dimensional COMSOL ®[48] based FE model was developed to compute the dispersion curve of the coupled model, i.e, the aluminum plate and the PZT transducer, as illustrated in Fig. 4. Floquet boundary conditions were then applied at side boundaries of the model to simulate the periodicity of the waveguide in the aluminum plate.

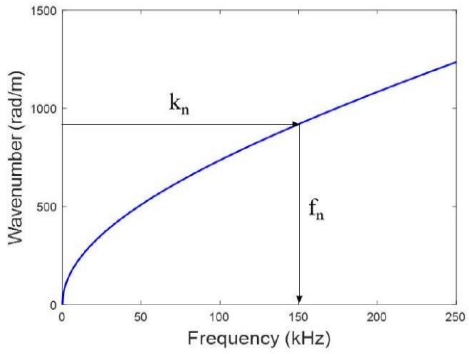

Figure 3: Dispersion relation of 1-mm-thick aluminum plate and determination of the A0 mode actuation frequency f_n associated with a wavenumber k_n

The domains were discretized using quadrilateral elements with the size of $0.5\ \mathrm{mm}$ so that the shortest wavelength at the highest desired frequency is precisely modeled. The Eigenfrequency analysis along with a user-defined wavenumber sweep were then employed to compute the dispersion curve of the considered model.

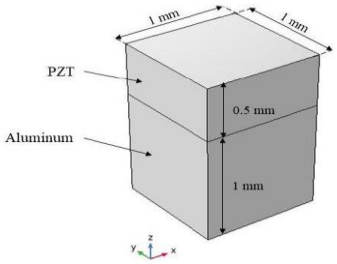

Figure 4: Geometry of the model used for dispersion calculation.

As shown in Fig. 5a, a significant difference in the dispersion curves of the given cases, i.e., the aluminum plate with-PZT and without-PZT, is observed. Consequently, the wavenumber associated with the specific excitation frequency will be changed, leading to a different wave direction, hence a different steering angle (see Fig. 5b). In order to shed light on the interpretation of the results, a comparison of beampatterns for two different frequencies of $100\mathrm{kHz}$ and $250\mathrm{kHz}$ was performed. As depicted in Fig. 6, the radiation directions for the given cases are different, confirming the need for a dispersion correction procedure.

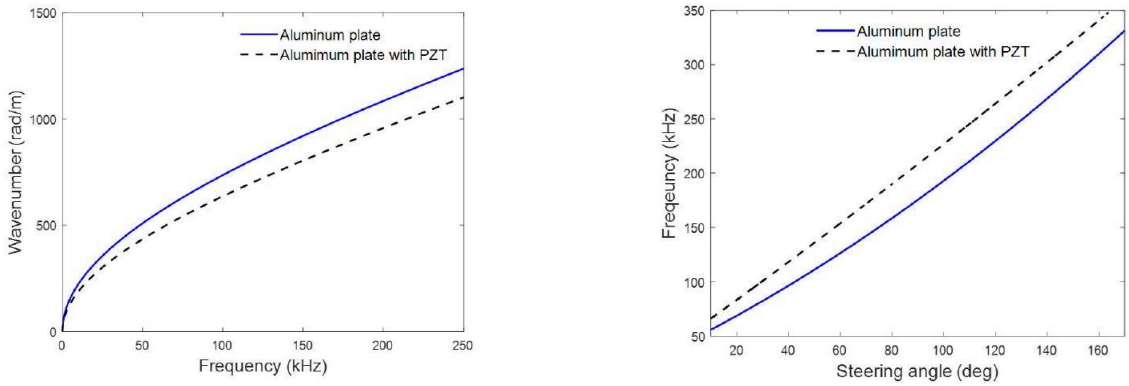

(a) (b)

Figure 5: a) comparison of the dispersion curves for the aluminum plate with-PZT and without-PZT b) corresponding frequency-angle map

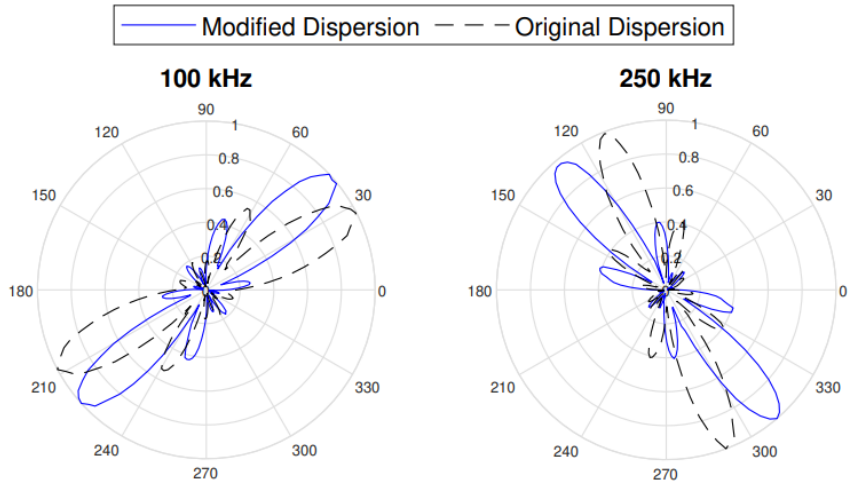

Figure 6: Comparison of the normalized beampatterns predicted by the analytical model using the original and modified dispersion relation at two different frequencies.

5. MODELING OF FREQUENCY STEERABLE ACOUSTIC TRANSDUCERS

Modelling the interaction of piezoelectric transducers and guided waves requires the setup and solution of a system of coupled partial differential equations [49]. More specifically, the generation of electrical charges resulting from the deformation of the piezoelectric material demands a simultaneous solving of both the electrical and structural mechanics constitutive equations [41]. Due to the complexity of the analytical models, the solution of these equations in complex geometrical domain is generally pursued via numerical techniques.

The numerical solutions of guided waves generated by PZT transducers can be obtained using a variety of methods, including Finite element method (FEM), Finite difference method (FDM), Elastic Finite integration technique (EFIT) and spectral FEM (SFEM) [50]. In this work, we resort to the Finite Element (FE) based simulations implemented in the commercial software COMSOL Multiphysics ® [48].

The coupled piezoelectric equations employ the direct and inverse piezoelectric effects to link the structural deformation with the electric response of the material [41]. More in detail, as described in [49], the mechanical and electrical behavior of piezoelectric materials are described by the following linear equations:

$$S_{ij} = s^{E}_{ijkl} T_{kl} + d_{kij} E_k \qquad (9)$$
$$D_j = d_{jkl} T_{kl} + \epsilon^{T}_{jk} E_k$$

where s^{E}_{ijkl} indicates the mechanical compliance of the material measured at zero electric field $E = 0$, ϵ^{T}_{jk} defines the dielectric permittivity measured at zero mechanical stress $T = 0$, and d_{kij} refers to the piezoelectric coupling effects. S_{ij} is the mechanical strain and D_j denotes the electrical displacement.

In the current study, a three-D FE model of FSAT has been developed using COMSOL Multiphysics and the two key mechanisms, i.e., structural mechanics and electrostatics, are coupled in the FE model to evaluate the FSAT directional performance. In order to validate the FSAT theoretical concept, the frequency domain analysis is adopted since the analytical approach is based on the steady-state analysis. The simulation is further expanded to the time domain analysis to investigate the influence of a transient regime on the directionality of the device.

TABLE I: Elastic and piezoelectric properties of the materials used in the simulation.

	Aluminum	Epoxy Glue	PIC-255
Density, $\rho[\mathrm{kg/m^3}]$	2750	1150	7800
Elastic modulus $[GPa]$	70	4.7	$C_{11} = C_{22} = 132.7$ $C_{12} = 86.67$ $C_{13} = C_{23} = 85.6$ $C_{33} = 119.2$ $C_{44} = C_{55} = 21.3$ $C_{66} = 22.9$
Poisson ratio	0.33	0.35	-
Piezoelectric constants, d_{kij} [C/N]	-	-	$d_{31} = -187 \times 10^{-12}$ $d_{33} = 400 \times 10^{-12}$ $d_{15} = 617 \times 10^{-12}$
Electrical permittivity, ϵ_{jk}	-	-	$\epsilon_{11} = 1852$ $\epsilon_{32} = 1751$

Wave propagation simulation in frequency response analysis has quite a few benefits such as requiring less computational resources and time, compared to time domain analysis. In this regard, an aluminum plate with dimensions $500\ \mathrm{mm} \times 500\ \mathrm{mm}$ and thickness $1\ \mathrm{mm}$ was used as the propagation medium. The FSAT was then modeled on top of a small plate made of piezoelectric materials with dimensions $80\ \mathrm{mm} \times 80\ \mathrm{mm}$ and thickness $0.5\ \mathrm{mm}$. As depicted in Fig. 7, the spiral geometry of the FSAT obtained in the design procedure [32] is printed over the PZT, which is properly glued to the aluminum plate. The bonding between the PZT and the aluminum plate was simulated by defining a thin elastic layer of $30[\mu\mathrm{m}]$. Table I shows the elastic and piezoelectric properties of the aluminum plate, PZT and the bonding layer. The polarization direction for the PZT element assumed towards the z-direction. The mechanical damping in the considered piezoelectric material was implemented using Isotropic Loss Factor with the value of $\eta_s = 0.006$, considering the Mechanical quality factor (Q_m) of 80 . In order to avoid the wave boundary reflection, Perfectly Matched Layer (PML) was set at four plate boundaries to absorb the incident radiations without generating back reflections. As for the boundary conditions of the transducer, the bottom surface of the PZT was grounded, and an electric potential boundary condition was used at the top part. For the rest of the PZT element, zero charge boundary conditions were applied.

The transducer domains were meshed with Free Triangular elements, whereas Free Quad elements were used for the aluminum plate. In an effort to reduce the computational complexity of the model, a swept mesh in the z-direction was then employed. The mesh size was considered as $\frac{1}{10}$ of the shortest possible wavelength of the $A0$ mode in the aluminum plate, as suggested in [51]. Considering the studied frequency range of 100-250 kHz, the mesh size of $0.5\ \mathrm{mm}$ and $1\ \mathrm{mm}$ were utilized for the transducer and the aluminum plate, respectively. It is worth noting that the PML domains were meshed using Free Triangular elements with increasing mesh size at a low growth rate of 1.2, ensuring a reasonable mesh element quality.

The employed frequency domain analysis is based on the steady-state response of the waveguide subjected to a harmonic excitation. In this context, the simulations were conducted for six central frequencies of $100\mathrm{kHz}, 150\mathrm{kHz}, 180\mathrm{kHz}, 200\mathrm{kHz}, 220\mathrm{kHz}$ and $250\mathrm{kHz}$ according to the previous research [32].

To validate the simulation method, the simulation results including the generated wavefield and beampatterns are presented. The out-of-plane displacement field obtained from the frequency response analysis at different frequencies is utilized to show the effectiveness of the simulation method. The generated wavefield for the considered frequencies confirms the FSAT directional performance in the actuation mode, as shown in Fig. 8. Furthermore, radiation patterns for the frequencies of interest are assessed by generating polar plots with the absolute

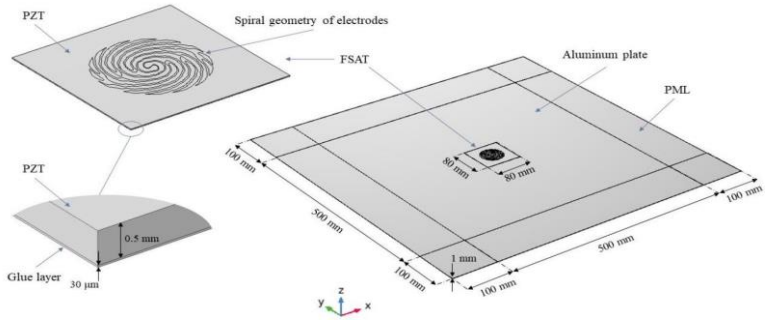

Figure 7: Three-dimensional geometry of the model in the frequency domain simulation

values of the displacement field. To do so, the out-of-plane displacement fields are extracted over a circle with a radius of $200\ \mathrm{mm}$ centered at the FSAT location, considering far field radiation. Fig. 9 displays the comparison of the measured directivity with the one predicted by the analytical model. A notably good agreement between them is observed, showing the correctness and robustness of the developed FE model.

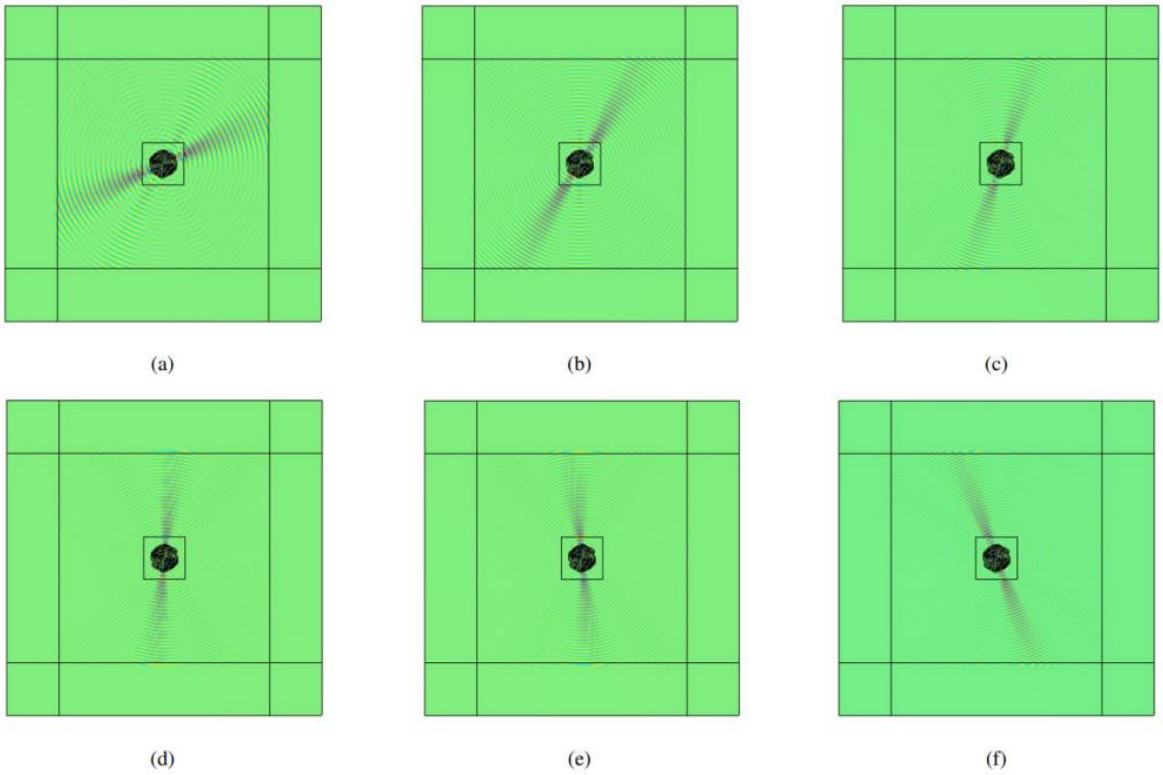

Figure 8: The generated wavefield by the FSAT at different frequencies (obtained from the frequency domain simulation): a) 100 kHz; b) 150kHz c) 180kHz;) 200kHz; e) 220kHz; f) 250kHz

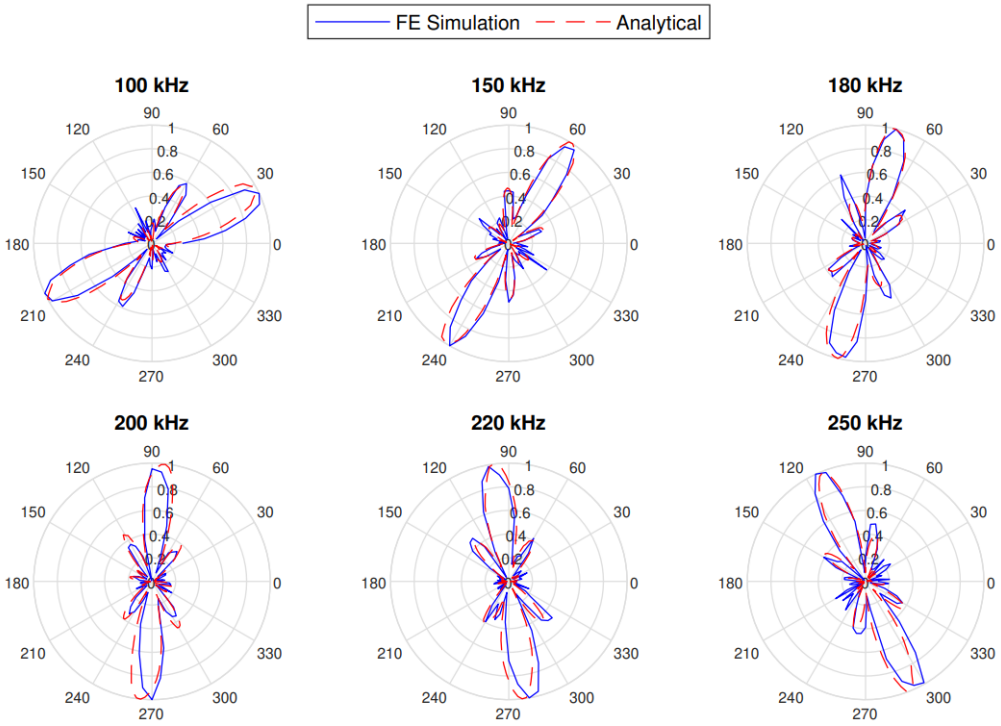

Figure 9: Comparison of the analytical and FE simulation normalized beampatterns in different frequencies (obtained from the frequency domain simulation)

For further validate of the concept, the transient analysis is carried out to simulate the guided wave propagation in the plate structure. The propagation medium was considered as an aluminum plate with

dimensions $400\ \text{mm} \times 400\ \text{mm} \times 1\ \text{mm}$, on which the FSAT is bonded in the same way as before. The electrical boundary condition of the transducer is also defined in the same fashion as the time analysis model. Contrary to the previous simulation, low-reflecting boundary conditions were utilized at side boundaries instead of PMLs to reduce wave-back reflections. Such an alternative approach was implemented to reduce the computational cost of the numerical model due to the complexity of the PML formulation in time analysis. It should be noted that the aluminum plate and the transducer components were meshed with the same method as the frequency domain simulation.

For the simulation purposes, a 5-cycles Hanning-windowed sine burst excitation signal with $10\ \text{V}$ amplitude was applied to the FSAT electrode domains to generate the Lamb wave. The employed function to generate such a signal is given by Equation (11):

$$V_{\text{exc}} = \frac{A}{2}\left(1 - \cos\left(\frac{\omega t}{N}\right)\right)\sin(\omega t)\left(t < \frac{N}{f}\right) \tag{10}$$

in which, A is the signal amplitude, N stands for the number of cycles, f denotes the excitation frequency, t is the time and ω indicates the angular frequency. The excitation signal along with the corresponding frequency spectrum for the frequency of 200kHz is depicted in Fig. 10. Transient analysis demands a suitable integrating time step to ensure numerical stability as well as to reduce the computation time. In order to identify the appropriate time step for the transient study, the Courant-Friedrichs-Lewy (CFL) condition [51] was used. As recommended in [51], a CFL value of 0.2 was considered for the guided wave problem. The Generalized- α solver was then chosen for the transient analysis.

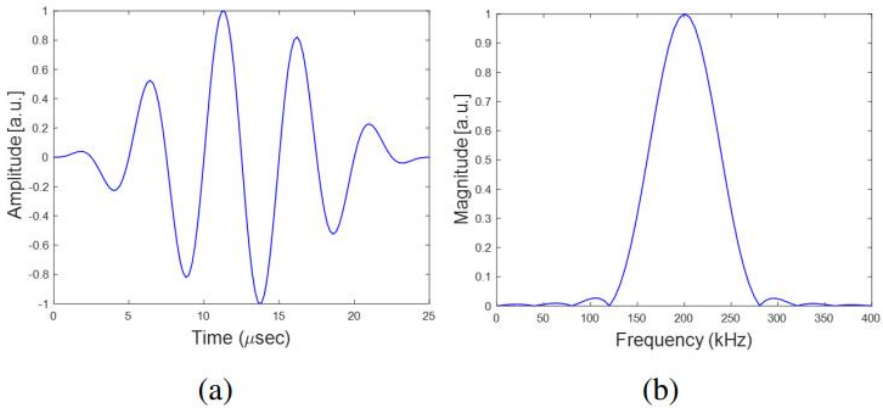

Figure 10: a) 5-cycles Hanning-windowed excitation signal with a center frequency of 200kHz b) corresponding frequency spectrum

The simulation results are reported in Fig. 11 in terms of out-of-plane displacement at specific time instant for three burst centers frequencies of 100kHz, 150kHz, and 200 kHz. The snapshots of the wavefield generated by the FSAT at successive time instants are presented in Fig. 11, clearly indicating the directional performance of the simulated FSAT. Furthermore, radiation patterns are presented in terms of time Root Mean Square (RMS) of the out-of-plane displacement, which is extracted on a circular grid of $150\ \text{mm}$ radius around the transducer. Fig. 12 demonstrates the comparison of the results with the predicted beampatterns resulted from the analytical model.

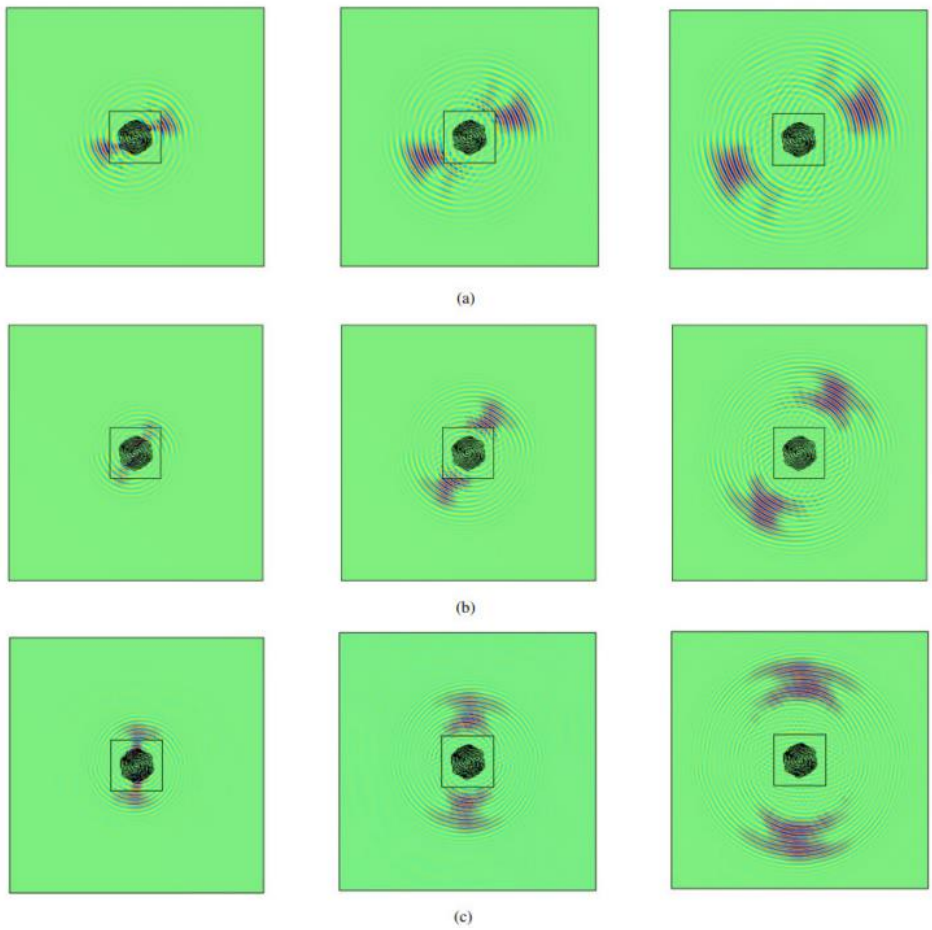

Figure 11: Snapshots at successive time instants of wavefield (left to right: $30\mu s, 50\mu s, 70\mu s$) generated by the FSAT at different frequencies: a) 100kHz; b) 150kHz c) 200kHz

As it can be seen, the FE simulation results are in a very good agreement with the analytical predictions. It is worth noting that the FEM beampattern is wider than the one associated with the analytical model. The reason for such a difference lies in the different approaches used for computing the directionality function. More in detail, the analytical function is extracted for a single frequency, i.e., the central frequency of the excitation signal. In contrast, in the FE model, the directivity function is related to the entire spectrum of the excitation signal, which encompasses a narrow region around its central frequency, resulting in a wider directionality beam. In order to mitigate such an effect, an excitation signal with more cycles, e.g., 10 cycles, can be implemented for the transient analysis.

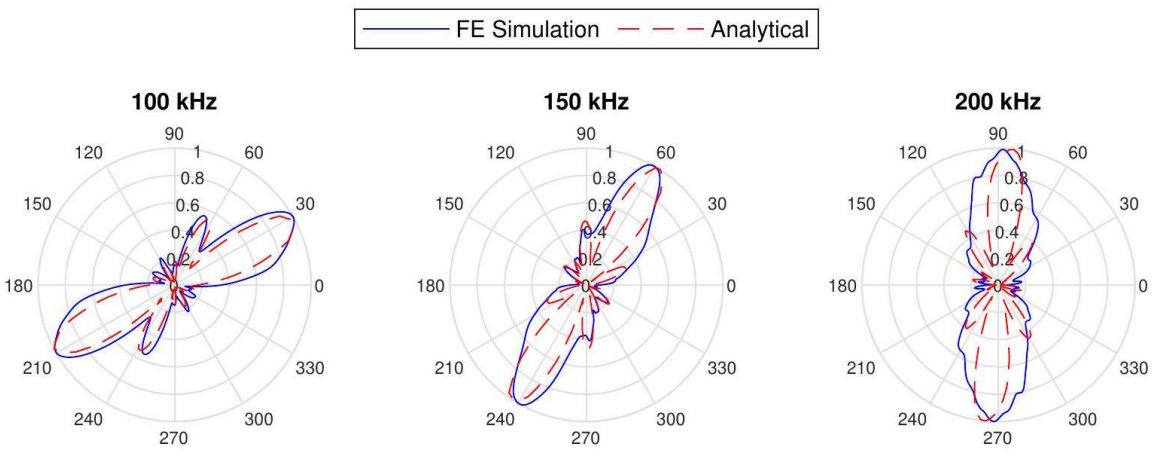

Figure 12: Comparison of the analytical and FE simulation normalized beampatterns at different frequencies (obtained from the time domain simulation)

6. EXPERIMENTAL TESTING

In this section, the fabrication technique utilized for the manufacturing of FSAT electrode shapes is outlined first. The experimental tests performed to assess the actuation capabilities of the device are then described.

The core material of the proposed FSAT design is based on PIC 255 material from PI Ceramic (Lederhose, Germany). Quadratic plates with a side length of 80 mm and a thickness of 0.5mm have been used for fabrication. The quadratic shape has been maintained to avoid additional costs required for laser cutting to achieve a circular shape. Electrodes have been applied to the PZT plates by screen-printing using silver paste, with one side applied over the entire surface and one side textured. After fixing the electrodes, the PZT plates are poled over the plate thickness.

In order to experimentally validate the FSAT directional performance, the fabricated FSAT was used for testing in actuation mode. The inspected structure is a 1mm thick aluminium plate of dimensions 1000 mm × 1000 mm, to which the FSAT prototype is attached through epoxy resin (EPO-TEK 301-2) with a thickness of 20-50 µm. As shown in Fig. 13a, the experimental system is composed of a signal generator (Tektronix AFG 3022B), a power amplifier (Tegam 2350), a digital oscilloscope (Tektronix DPO 3014), and a Scanning Laser Doppler Vibrometer (SLDV) (OptoMET) equipped with a personal computer. SLDV is capable of precisely measuring surface wave motion, enabling a non-contact and rapid guided waves sensing and visualization [52]. In this test, the SLDV was positioned perpendicularly to the plate in a way that the plate out-of-plane displacements were recorded.

Two types of experiments were carried out to comprehensively investigate the FSAT performance. In the first experiment, a rectangular area of 150 mm × 250 mm was considered as the scanning region, as depicted in Fig. 13b. The inspection area was then discretized in a proper number of spatial grid points (100×60) considering the computer memory as well as the imaging resolution. Sinusoidal signals with 1 ms duration and 10 V peak-to-peak amplitude were generated to excite the transducer in the selected frequencies. It should be noted that the input signal was provided as a voltage difference, which is connected to the positive and negative electrodes of the FSAT through a wire (see Fig. 13b).

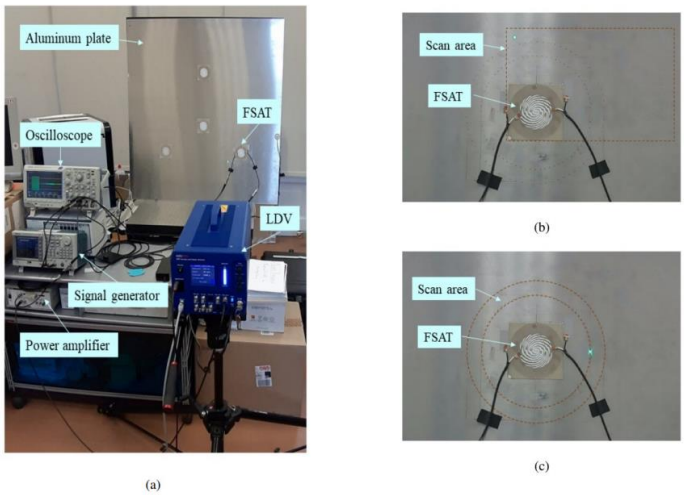

Figure 13: The FSAT actuating experiment. a) the overall test setup, b) the scan region (square) in the first experiments, c) the scan region (ring) in the second experiments

The experimental wavefield recorded by the SLDV are compared with the corresponding FE simulation data. As shown in Fig. 14, the experimental results show a very good agreement with the simulation in the selected frequencies. It is worthwhile to mention that the wavefield image obtained from the FE simulation at 200kHz is regulated to be compatible with the SLDV results, due to the limited resolution of the image acquisition system.

In the second experiment, the scanning region was changed to a circular ring cantered at the FSAT location to evaluate the wavefield (see Fig. 13c). The inner and outer radius of the ring is 10 mm and 12 mm, respectively. Such a grid provides the opportunity to visualize the directivity pattern around the transducer in a faster manner. In this test, 10cycle sine signals modulated by a Hanning window with 10 V peak-to-peak amplitude were generated to excite the transducer at the selected frequencies in order to obtain the directivity patterns.

Radiation patterns are reported in terms of the RMS value of the out-of-plane displacement, which is extracted over the outer radius of the ring region. As displayed in Fig. 15, the radiation directions are in a very good agreement with those obtained from the FE simulation. It should be noted that the directivity patterns of the FE model are extracted over a circle with the same radius as of the experimental one. There is a slight discrepancy in the amplitude of the main lobes, which can be attributed to the reflections from the plate boundaries.

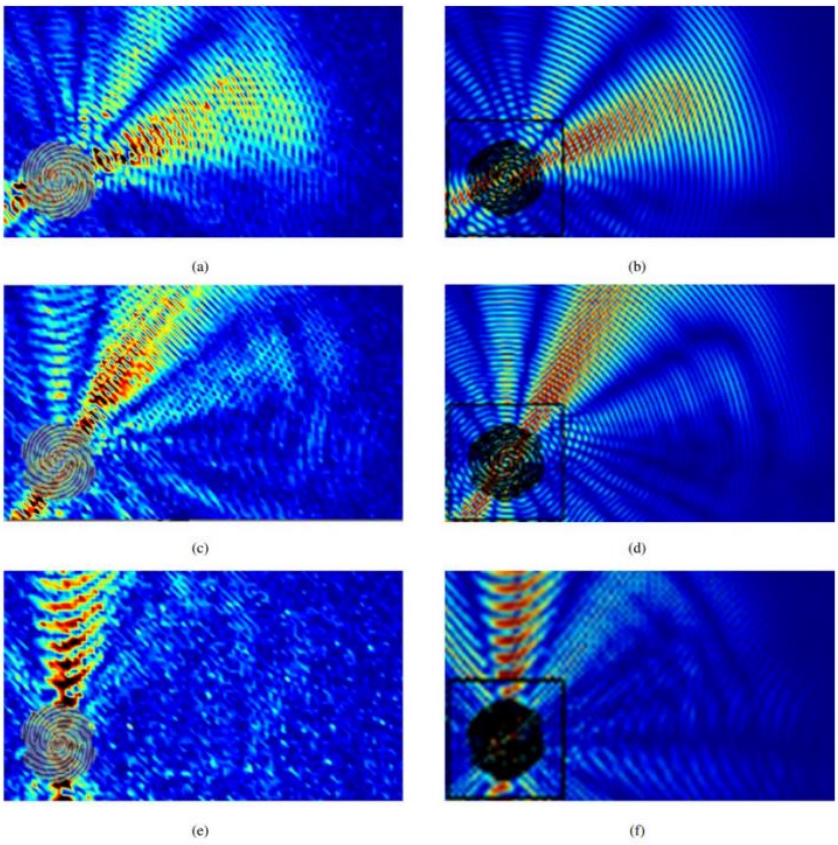

Figure 14: Snapshots of the displacement wavefield generated by the FSAT at the same time instants for SLDV experiment (left) and FE simulation (right) at different frequencies: a,b) 100kHz; c,d) 150kHz; e,f) 200kHz

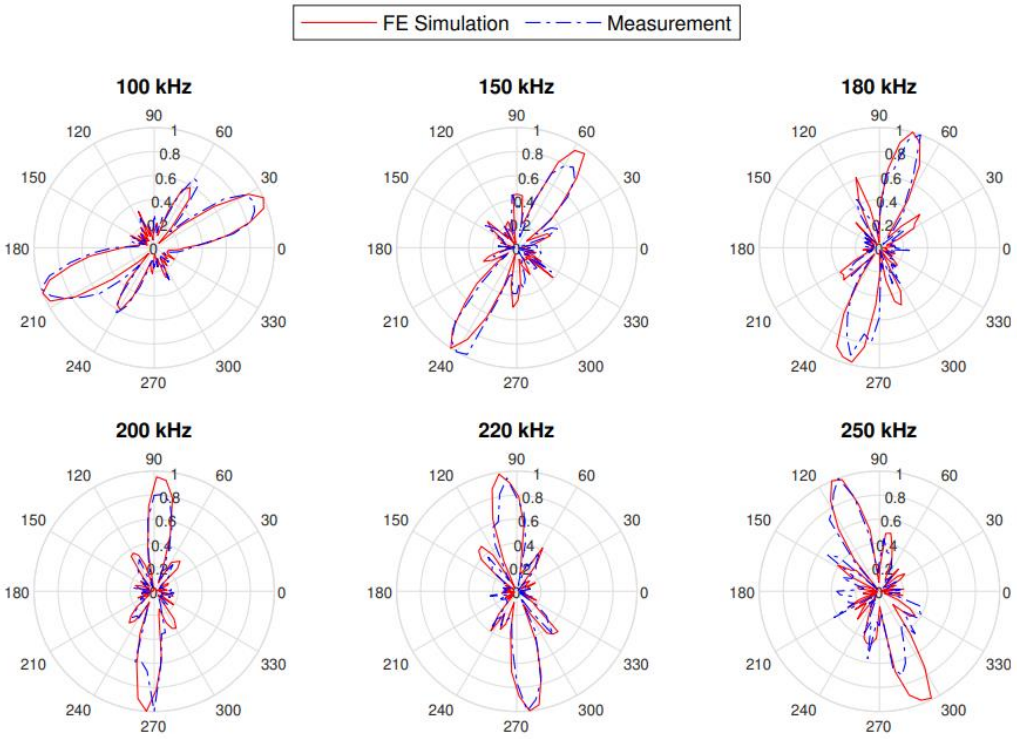

Figure 15: Normalized simulated and measured radiation patterns at different frequencies

7. CONCLUSION

The design, simulation, and experimental characterization of a novel type of Frequency Steerable Acoustic Transducers (FSATs) for guided waves actuation in a plate-like structure were reported in this study. In the previous spiral shaped FSAT examples, PVDF was used for transducer manufacturing, which had shown a limited directionality due to the low actuation strength of PVDF. This work, by contrast, demonstrated the capability of Piezoceramics to outperform PVDF in terms of guided wave actuation. The preliminary numerical results revealed very substantial differences in the radiation patterns between the two examples, that is, the PVDF FSAT and the Piezoceramic FSAT, which was due to the different coupling behavior with the host structure. As the effect of the transducer thickness (hence stiffness) was not taken into consideration in the previous FSAT design, a FE model was developed to obtain the dispersion curve of the coupled structure to modify the FSAT design procedure. Radiation patterns predicted by the modified analytical model were verified by means of the FE COMSOL Multiphysics models considering both the steady-state and the transient analysis. For practical realization, the proposed Piezoceramic FSAT was fabricated by the screen-printing technique. Finally, the device was validated experimentally by implementing SLDV experiments. The results showed excellent performance of the proposed device in the actuation mode.

The limitation faced by the current device is a 180° ambiguity, due to which waves are excited in two opposite directions simultaneously. Such limitations might be addressed in future studies, which are being undertaken by the authors.

8. REFERENCES

[1] Ajay Raghavan and Carlos ES Cesnik. Piezoelectric-actuator excited- wave field solutions for guided-wave structural health monitoring. In *Smart Structures and Materials 2005: Sensors and Smart Structures Technologies for Civil, Mechanical, and Aerospace Systems*, volume 5765, pages 313–323. International Society for Optics and Photonics, 2005.

[2] Jochen Moll, Jens Kathol, Claus-Peter Fritzen, Maria Moix-Bonet, Mar- cel Rennoch, Michael Koerdt, Axel S Herrmann, Markus GR Sause, and Martin Bach. Open guided waves: online platform for ultrasonic guided wave measurements. *Structural Health Monitoring*, 18(5-6):1903–1914, 2019.

[3] Alessandro Marzani, Nicola Testoni, Luca De Marchi, Marco Messina, Ernesto Monaco, and Alfonso Apicella. An open database for bench- marking guided waves structural health monitoring algorithms on a com- posite full-scale outer wing demonstrator. *Structural Health Monitoring*, 19(5):1524–1541, 2020.

[4] BC Lee and WJ Staszewski. Modelling of lamb waves for damage detection in metallic structures: Part i. wave propagation. *Smart materials and structures*, 12(5):804, 2003.

[5] JH Nienwenhui, John J Neumann, David W Greve, and Irving J Oppenheim. Generation and detection of guided waves using pzt wafer transducers. *IEEE transactions on ultrasonics, ferroelectrics, and frequency control*, 52(11):2103–2111, 2005.

[6] Zhiyuan Shen, Shuting Chen, Lei Zhang, Kui Yao, and Chin Yaw Tan. Direct-write piezoelectric ultrasonic transducers for non-destructive testing of metal plates. *IEEE Sensors Journal*, 17(11):3354–3361, 2017.

[7] Jochen Moll, Mikhail V Golub, Evgeny Glushkov, Natalia Glushkova, and Claus-Peter Fritzen. Non-axisymmetric lamb wave excitation by piezoelectric wafer active sensors. *Sensors and Actuators A: Physical*, 174:173–180, 2012.

[8] Pan Hu, Haitao Wang, Guiyun Tian, Zeyu Dong, Fasheng Qiu, and Billie F Spencer. Wireless localization of spallings in switch-rails with guided waves based on a time–frequency method. *IEEE Sensors Journal*, 19(23):11050–11062, 2019.

[9] Sina Fateri, Premesh Shehan Lowe, Bhavin Engineer, and Nikolaos V Boulgouris. Investigation of ultrasonic guided waves interacting with piezoelectric transducers. *IEEE Sensors Journal*, 15(8):4319–4328, 2015.

[10] Luca De Marchi, Massimo Ruzzene, Buli Xu, Emanuele Baravelli, and Nicolo Speciale. Warped basis pursuit for damage detection using lamb waves. *IEEE transactions on ultrasonics, ferroelectrics, and frequency control*, 57(12):2734–2741, 2010.

[11] Jochen Moll, RT Schulte, B Hartmann, CP Fritzen, and O Nelles. Multi- site damage localization in anisotropic plate-like structures using an active guided wave structural health monitoring system. *Smart materials and structures*, 19(4):045022, 2010.

[12] Z Sharif Khodaei and MH Ferri Aliabadi. Damage detection and characterization with piezoelectric transducers: Active sensing. In *Structural Health Monitoring for Advanced Composite Structures*, pages 1–46. World Scientific, 2018.

[13] Danilo Ecidir Budoya, Leandro Melo Campeiro, and Fabricio Guimaraes Baptista. Sensitivity enhancement of piezoelectric transducers for impedance-based damage detection via a negative capacitance interface. *IEEE Sensors Journal*, 20(23):13892–13900, 2019.

[14] Maciej Radzien´ski, Paweł Kudela, Alessandro Marzani, Luca De Marchi, and Wiesław Ostachowicz. Damage identification in various types of composite plates using guided waves excited by a piezoelectric transducer and measured by a laser vibrometer. *Sensors*, 19(9):1958, 2019.

[15] Jun Wu, Xuebing Xu, Cheng Liu, Chao Deng, and Xinyu Shao. Lamb wave-based damage detection of composite structures using deep convolutional neural network and continuous wavelet transform. *Composite Structures*, 276:114590, 2021.

[16] Harry L Van Trees. *Optimum array processing: Part IV of detection, estimation, and modulation theory*. John Wiley & Sons, 2004.

[17] Jian Li and Joseph L Rose. Implementing guided wave mode control by use of a phased transducer array. *IEEE transactions on ultrasonics, ferroelectrics, and frequency control*, 48(3):761–768, 2001.

[18] Sevan Harput and Ayhan Bozkurt. Ultrasonic phased array device for acoustic imaging in air. *IEEE sensors journal*, 8(11):1755–1762, 2008.

[19] Lingyu Yu and Victor Giurgiutiu. In situ 2-d piezoelectric wafer active sensors arrays for guided wave damage detection. *Ultrasonics*, 48(2):117–134, 2008.

[20] Kumar Anubhav Tiwari, Renaldas Raisutis, Liudas Mazeika, and Vyk- intas Samaitis. 2d analytical model for the directivity prediction of ultrasonic contact type transducers in the generation of guided waves. *Sensors*, 18(4):987, 2018.

[21] Howard M Matt and Francesco Lanza di Scalea. Macro-fiber composite piezoelectric rosettes for acoustic source location in complex structures. *Smart Materials and Structures*, 16(4):1489, 2007.

[22] Vincent Laude, Davy Ge´rard, Naima Khelfaoui, Carlos F Jerez-Hanckes, Sarah Benchabane, and Abdelkrim Khelif. Subwavelength focusing of surface acoustic waves generated by an annular interdigital transducer.

[23] Chao Wang, Zheyao Wang, Tian-Ling Ren, Yiping Zhu, Yi Yang, Xiaoming Wu, Haining Wang, Huajun Fang, and Litian Liu. A mi- cromachined piezoelectric ultrasonic transducer operating in d_{33} mode using square interdigital electrodes. *IEEE sensors journal*, 7(7):967– 976, 2007.

[24] KI Salas and Carlos ES Cesnik. Guided wave excitation by a clover transducer for structural health monitoring: theory and experiments. *Smart Materials and Structures*, 18(7):075005, 2009.

[25] Tadeusz Stepinski, Michał Man´ka, Adam Martowicz, and Vivek T Rathod. Interdigital transducers in structural health monitoring based on lamb waves: a state of the art. In *Sensors and Smart Structures Technologies for Civil, Mechanical, and Aerospace Systems 2016*, vol- ume 9803, pages 176–190. SPIE, 2016.

[26] Tadeusz Stepinski, Michał Man´ka, and Adam Martowicz. Interdigital lamb wave transducers for applications in structural health monitoring. *NDT & E International*, 86:199–210, 2017.

[27] Michał Man´ka, Mateusz Rosiek, Adam Martowicz, Tadeusz Stepinski, and Tadeusz Uhl. Pzt based tunable interdigital transducer for lamb waves based ndt and shm. *Mechanical Systems and Signal Processing*, 78:71–83, 2016.

[28] Bernd Ko¨hler, Yongtak Kim, Konrad Chwelatiuk, Kilian Tscho¨ke, Frank Schubert, and Lars Schubert. A mode-switchable guided elastic wave transducer. *Journal of Nondestructive Evaluation*, 39(2):1–13, 2020.

[29] M Romanoni, S Gonella, N Apetre, and M Ruzzene. Two-dimensional periodic actuators for frequency-based beam steering. *Smart materials and structures*, 18(12):125023, 2009.

[30] Matteo Senesi, Buli Xu, and Massimo Ruzzene. Experimental char- acterization of periodic frequency-steerable arrays for structural health monitoring. *Smart Materials and Structures*, 19(5):055026, 2010.

[31] Matteo Senesi and Massimo Ruzzene. A frequency selective acoustic transducer for directional lamb wave sensing. *The Journal of the Acoustical Society of America*, 130(4):1899–1907, 2011.

[32] Matteo Senesi, Emanuele Baravelli, Luca De Marchi, and Massimo Ruzzene. Experimental demonstration of directional gw generation through wavenumber-spiral frequency steerable acoustic actuators. In *2012 IEEE International Ultrasonics Symposium*, pages 2694–2697. IEEE, 2012.

[33] RSC Monkhouse, PD Wilcox, and P Cawley. Flexible interdigital pvdf transducers for the generation of lamb waves in structures. *Ultrasonics*, 35(7):489–498, 1997.
[34] X Lin and FG Yuan. Diagnostic lamb waves in an integrated piezoelec- tric sensor/actuator plate: analytical and experimental studies. *Smart Materials and Structures*, 10(5):907, 2001.
[35] Vinicius Augusto Dare´ de Almeida, Fabricio Guimara˜es Baptista, and Paulo Roberto de Aguiar. Piezoelectric transducers assessed by the pencil lead break for impedance-based structural health monitoring. *IEEE Sensors Journal*, 15(2):693–702, 2014.
[36] Daniel Schmidt, Michael Sinapius, and Peter Wierach. Design of mode selective actuators for lamb wave excitation in composite plates. *CEAS Aeronautical Journal*, 4(1):105–112, 2013.
[37] Leandro Melo Campeiro, Danilo Ecidir Budoya, and Fabricio Guimara˜es Baptista. Lamb wave inspection using piezoelectric diaphragms: an initial feasibility study. *Sensors and Actuators A: Physical*, page 112859, 2021.
[38] Lorenzo Capineri and Andrea Bulletti. Ultrasonic guided-waves sensors and integrated structural health monitoring systems for impact detection and localization: A review. *Sensors*, 21(9):2929, 2021.
[39] B Lin and Victor Giurgiutiu. Modeling and testing of pzt and pvdf piezoelectric wafer active sensors. *Smart Materials and Structures*, 15(4):1085, 2006.
[40] Emanuele Baravelli, Matteo Senesi, Massimo Ruzzene, Luca De Marchi, and Nicolo Speciale. Double-channel, frequency-steered acoustic transducer with 2-d imaging capabilities. *IEEE transactions on ultrasonics, ferroelectrics, and frequency control*, 58(7):1430–1441, 2011.
[41] Markus GR Sause, Marvin A Hamstad, and Siegfried Horn. Finite ele- ment modeling of conical acoustic emission sensors and corresponding experiments. *Sensors and Actuators A: Physical*, 184:64–71, 2012.
[42] Matteo Senesi. *Frequency steerable acoustic transducers*. Georgia Institute of Technology, 2012.
[43] Matteo Carrara and Massimo Ruzzene. Structural health and strain monitoring sensing through fourier-based transducers. *Mechanics of Advanced Materials and Structures*, 22(1-2):67–76, 2015.
[44] L De Marchi, N Testoni, and A Marzani. Spiral-shaped piezoelectric sensors for lamb waves direction of arrival (doa) estimation. *Smart Materials and Structures*, 27(4):045016, 2018.
[45] Marco Dibiase, Masoud Mohammadgholiha, and Luca De Marchi. Opti- mal array design and directive sensors for guided waves doa estimation. *Sensors*, 22(3):780, 2022.
[46] Matteo Carrara and Massimo Ruzzene. Fourier-based design of acoustic strain rosettes. In *Sensors and Smart Structures Technologies for Civil, Mechanical, and Aerospace Systems 2014*, volume 9061, page 906135. International Society for Optics and Photonics, 2014.
[47] Christopher Hakoda, Joseph Rose, Parisa Shokouhi, and Clifford Lis- senden. Using floquet periodicity to easily calculate dispersion curves and wave structures of homogeneous waveguides. In *AIP Conference Proceedings*, volume 1949, page 020016. AIP Publishing LLC, 2018.
[48] COMSOL Multiphysics v. 5.6. www.comsol.com. COMSOL AB, Stock- holm, Sweden.
[49] Victor Giurgiutiu and Andrei N Zagrai. Characterization of piezoelectric wafer active sensors. *Journal of Intelligent Material Systems and Structures*, 11(12):959–976, 2000.
[50] Vincentius Ewald, Ramanan Sridaran Venkat, Aadhik Asokkumar, Rinze Benedictus, Christian Boller, and Roger M Groves. Perception modelling by invariant representation of deep learning for automated structural diagnostic in aircraft maintenance: A study case using deepshm. *Me- chanical Systems and Signal Processing*, 165:108153, 2022.
[51] Bikash Ghose, Krishnan Balasubramaniam, CV Krishnamurthy, and A Subhananda Rao. Two dimensional fem simulation of ultrasonic wave propagation in isotropic solid media using comsol. In *COMSOL Conference*, volume 37, page 38, 2010.
[52] Michelangelo Maria Malatesta, Jochen Moll, Pawel Kudela, Maciej Radzien´ski, and Luca De Marchi. Wavefield analysis tools for wavenumber and velocities extraction in polar coordinates. *IEEE Transactions on Ultrasonics, Ferroelectrics, and Frequency Control*, 69(1):399–410, 2021.